



Cairns, J., Vezza, M., Green, R. and MacVicar, D. (2021) Numerical optimisation of a Ship Wind-Assisted Propulsion system using blowing and suction over a range of wind conditions. *Ocean Engineering*, 240, 109903. (doi: [10.1016/j.oceaneng.2021.109903](https://doi.org/10.1016/j.oceaneng.2021.109903))

There may be differences between this version and the published version. You are advised to consult the publisher's version if you wish to cite from it.

<http://eprints.gla.ac.uk/253456/>

Deposited on 13 October 2021

Enlighten – Research publications by members of the University of Glasgow
<http://eprints.gla.ac.uk>

Numerical optimisation of a Ship Wind-Assisted Propulsion system using blowing and suction over a range of wind conditions

James Cairns^{a,*}, Marco Vezza^a, Richard Green^a and Donald MacVicar^b

^a*Aerospace Sciences Research Division, James Watt Building, University of Glasgow, Glasgow, G12 8QQ, UK (phone: +44 141 330 2032)*

^b*SMAR Azure LTD, 14-18 Hill Street, Edinburgh, EH2 3JZ, UK (phone: +44 131 610 7627)*

ARTICLE INFO

Keywords:

CFD
Circulation control
Coflow jet
Robust optimization
Surrogate model
Wingsail

ABSTRACT

A Kriging surrogate model and a genetic algorithm are used to optimise the geometry of a ship wind assisted propulsion system (SWAP). The SWAP device is an actively controlled aerofoil mounted vertically on the deck of a ship in order to produce a forward propulsive force from the wind. The SWAP concept uses a circulation control system which employs both blowing from the leading edge and suction from the trailing edge. The aerodynamic parameters of the sail are found using a computational fluid dynamics (CFD) model validated against experimental data for a similar system, the coflow jet aerofoil. Further application of Kriging models is used to predict maximum lift coefficients for multiple freestream velocities, ensuring that the optimised device offers robust performance and low sensitivity to expected variations in wind speed. The maximum achievable lift coefficient was found to be 13.17% greater than for the baseline aerofoil over a range of wind speeds from 8-12m/s.

1. Introduction

The shipping industry is accountable for approximately 90% of worldwide trade and is essential for the global economy (Hoffmann and Sirimanne, 2017). Although, relative to road transport and aviation, shipping represents a more greenhouse gas (GHG) efficient means of transportation, the sheer scale of the shipping industry results in a major contribution to worldwide GHG emissions. In the energy and environment conscious world of today, where there is an ever-increasing focus on reducing these emissions, shipping represents an area where significant reductions can be realised.

Research published by the International Maritime Organisation (IMO) in 2014 estimates total shipping emissions to be approximately 796 million tonnes, accounting for 2.2% of worldwide output. If left to develop at the current rate, Cames et al. (2015) have estimated that shipping emissions will increase between 50% - 250% between 2012 and 2050 and could represent up to 17% of global CO₂ output.

As a result, major legislation changes are being introduced to perhaps instigate a movement away from traditional fossil fuel based propulsion systems and towards cleaner alternatives. The IMO have tightened restrictions on sulphur dioxide emissions by stipulating that fuels must have a maximum sulphur content of no more than 0.5 m/m (mass by mass). This change is just one aspect of a wider IMO ambition to reduce shipping related greenhouse gas emissions by 70%, relative to the level in 2008, which will certainly mean further restrictive legislation is immanent (Joung et al., 2020).

In addition to this increasingly persuasive environmental case and the legislative changes that it has triggered, short term change may also be led by the economics of the situation. Interest in methods of ship propulsion which do not use

fossil fuels has historically been driven by rising oil prices. The first major investigation into wind ship propulsion in the modern age was catalysed by political instabilities during the 1970's and the resulting oil embargoes and significant price rises that they caused (Chrzanowski, 1980).

Between 1998 and 2020 oil prices had seen extended growth at a rate which surpassed even that of the 1970's oil crises, and although a Coronavirus led crash has since caused a price correction, such volatility can be equally disastrous to ship owners. Difficulties in future cost estimations and uncertainties in ensuring that turnovers cover costs may still cause ship operators to look at fossil fuel independent means of propulsion such as harvesting energy from the wind. This study investigates one such means of doing so and sets out to optimise the geometry of an actively controlled wingsail system titled SWAP.

2. Literature Review

2.1. Wind Ship Propulsion

For thousands of years humans have harvested wind power, be it from primitive sailboats dated to the 5th millennium BC, or by the vast wind turbine farms of today (Carter, 2006). Even still, there exists a huge amount of untapped, clean power available from the wind, especially over the large, flat and obstacle free ocean environment. The so-called 'Age of Sail', roughly dated from the 15th through to the mid-19th centuries, was the heyday of wind ship propulsion (Carter and Carter, 2010). During this time the sailing ship was king, superseding the oar propelled ships of previous times and instigating the Age of Discovery, allowing extensive overseas exploration and trade (Lang, 2006).

With transport ships powered solely by sail a thing of the past, the public image of such crafts today is largely governed by their portrayal in literature and media. Novels

*Corresponding author. E-mail address: j.cairns.1@research.gla.ac.uk

with a stylistic emphasis on heroism and adventure depict the so called ‘cool ship’, The Argo, The Hispaniola, The Black Pearl etc., and can conjure a rose-tinted and overly romantic image of the sailing ship in contrast to a much harsher and brutal reality. Ships in these times were extremely dangerous environments. Navigation of coastal and open waters, with complete reliance on favourable wind conditions, and no means of on demand propulsion left ships at the mercy of the unrelenting wrath of the sea. The invention of the steam engine changed this reality forever, with steam powered propellers quickly replacing sails and ending the dominance of wind power by decoupling the reliability of transport shipping from chaotic wind conditions.

Wind ship propulsion was recently reincarnated in the 1980’s by the previously mentioned oil price increases. The 1973 oil crisis in particular dramatically changed the existing shipping trends and initiated several government funded campaigns looking to find an alternative and feasible source of propulsion (Chrzanowski, 1980). The environment led shipping legislation of today is once again spiking interest in such technologies.

Rojon and Dieperink (2014) considered the current low market uptake for wind assisted propulsion systems for international shipping and identified the barriers and drivers for implementation. Their review of newspaper and academic articles as well as expert interviews classified the current knowledge development for two modern means of ship propulsion, kites and Flettner rotors, as low and as low/medium for sails, only due to the increased involvement of public research institutions for sail developments. Despite this, their classification for guidance of the search - a means of judging the promise of the technologies by evaluating the positivity of comment by authors reviewed in their literature study - was deemed medium to high. A leading barrier to the uptake of wind propulsion was a lack of practical knowledge and verified data available to ship owners. This led the authors to identify a ‘vicious circular’ problem - that in order to acquire this essential practical knowledge, owners must participate in trials and implement the technologies. Companies are unwilling to take on an initial untested investment but would eagerly profit from fuel savings if such a technology had been favourably implemented elsewhere. Rojon and Dieperink comment that this catch-22 situation requires the initiative of some brave frontrunners in order to be broken. Difficult economic times make this leap of faith unlikely and it becomes an issue requiring strong, decisive governance and increased political responsibility in order to promote the uptake of wind assisted technologies.

Atkinson et al. (2018) studied a wide range of issues regarding the use of wind assisted propulsion on modern ships. Their work balanced numerous strengths and weaknesses of wind ship propulsion but also considered some indirect effects of wind ship propulsion use often forgotten when approaching the subject from a purely cost savings and carbon reduction basis. These include benefiting the health of those living near ports and shipping lanes as well as enhancing the brand image and reputation of companies

that lead the way towards these cleaner alternatives. Some threats to widespread acceptance of wing sails were detailed. Among these, the shipping industry’s reputation for slow adaptation was highlighted, stating that resistance to wind ship propulsion may be met if shipping companies can satisfy regulatory requirements via existing technologies, even if they are not as efficient. Liquefied natural gas (LNG) was noted as a particular threat, offering a near zero sulphur content fuel with a reduced implementation cost. A fall in oil prices was also mentioned as a barrier to widespread operation, with specific reference to the abandonment of wind ship technologies after their initial bloom in the 1980’s. It remains to be seen whether this will repeat during current global conditions or whether the new IMO legislative changes will be sufficient to maintain interest.

2.1.1. Wingsails

A wingsail is a rigid, aerofoil like sail which can produce much higher lift forces than can be achieved using a conventional soft sail. Wingsails today are commonly seen in America’s Cup type racing crafts where their preferable lift to drag ratio has made them now a critical aspect of the sport. Recently there has been increasing interest in using wingsails for commercial shipping with one such research proposed vessel, the UT Wind Challenger studied by Ouchi et al. (2013), aimed at maximising ocean wind power for large cargo vessels. Their example ship pictured in Figure 1 used nine rigid sails with a sail area of 9000 m² as the main source of ship propulsion. Through computational fluid dynamics (CFD) analysis the authors showed that the wingsails were capable of propelling the ship at 14 kts at 12 m/s crosswind and that over an example route between Yokohama and Seattle, there was high probability of a fuel oil saving of between 20%-30%.



Figure 1: Artists impression of the UT Wind Challenger (Ouchi et al., 2013)

Viola et al. (2015) developed a wingsail set up for propulsion of a KVLCC2M hull. The KVLCC2M is a manufacturing driven modification on the classic KVLCC2 hull, a now standard shape conceived to provide CFD validation for a modern tanker ship with a bulbous bow. This hull shape has received extensive validation since its introduction in 1997. Viola et al expanded on the limitations of previous

studies which used low efficiency, rectangular curved plates for wing sections and instead used geometry inspired by the most recent America's Cup boats of the time. A genetic algorithm was used to optimise three parameters defining wingsail trim and rudder angle in order to minimise the required propeller thrust for a set ship speed. The work identified a maximum reduction in propeller thrust of 10% with optimal points identified when the ship sails across the wind. The propeller thrust reduction was found to have particular sensitivity to wingsail aspect ratio, leading the authors to comment that the most efficient set up would employ multiple tall wing sails rather than fewer which are short and wide.

Lee et al. (2016) developed an optimisation framework which couples numerical simulation with surrogate based optimisation methods to optimise parameters for multiple wingsails. Using the Spalart-Allmaras turbulence model for numerical analysis, they investigated the effect of flow interaction between wings and studied the propulsion effects of adding flap geometry. When considering multiple wingsails in tandem, the results show that thrust coefficients fell by 21-43% compared to a single sail in isolation. The study considered a fixed angle of attack at 8° for each wing meaning that the aerodynamic forces generated by the upstream wings acted to significantly decrease the local angle of attack for wings downstream. The smallest losses were found when the apparent wind direction was 90° to the wing. As a means of increasing the propulsive force of wingsails a surrogate model approach was used for optimisation. A trained Kriging model was coupled with a genetic algorithm to optimise relative angle of attack, flap length and flap deflection angle for three wings. Two dimensional results found thrust increases of between 14-22% and the method was shown to be equally applicable to three dimensional cases.

2.1.2. Kites

Having been initially viewed with some scepticism, the idea of using a towing kite is gaining some traction and several industrial parties are beginning to introduce designs. Differing from traditional sails in that they are attached to control lines rather than masts, kite rigs have many similarities with the kites used in wind sailing. Their double walled profile exhibits an aircraft-like wing shape in order to achieve high lift at low drag.

One of the first ships to use a kite for ship propulsion was the MV Beluga SkySails. The commercially operated SkySails system consists of a towing kite and combined control system for automated operation, launch and recovery (Rutkowski, 2016). The system boasts fuel savings of up to 20%, however externally validated data is hard to find (SkySails, 2020).

Along with increased interest in SkySails and other commercially operated kite propulsion systems, there has been increased research into towing kite optimal configuration and operation. Dadd et al. (2011) developed a mathematical model for predicting performance characteristics for kite

sails used as ship propulsion. It was reported that small figure of eight trajectories with a centre point orientated at 15° relative to the water line maximised propulsive benefit for the 300 m toe line studied. Horizontal orientations increased performance by a factor of 1.4 relative to vertical trajectories for downwind sailing. This was accounted for by allowing the kite to remain closer to the optimal elevation angle during the manoeuvre, however vertical orientations were preferred during close winded sailing when apparent wind directions need to be managed more closely. Similarly to the findings of Viola et al in their investigation of wing sail propulsion, the authors found particular sensitivity of propulsive force to aspect ratio. Increasing the kite aspect ratio from 4 to 5 was met with an increase in driving force of 15%, however the extent of this relationship was not studied. It was noted that smaller aspect ratios may be optimal from a stability point of view. Further work is required to investigate the exact trade off.

Naaijen and Koster (2007) conducted a performance study of kites as a means of auxiliary propulsion for merchant ships. The work evaluated possible fuel savings for certain environmental conditions but was not intended as an evaluation of the technologies practical feasibility, commenting that further work was required to fully investigate this aspect. For the cases studied, the optimal kite altitudes equalled approximately 30% of the towing line length and attachment at the bow minimised the required rudder angles. The authors found that the additional drift angle and ship resistance caused by wind speed and direction influencing the kite force were small for the majority of cases. These losses were counteracted by an improvement in the open water propeller efficiency and a theoretical fuel saving of up to 50% was found for the studied 50,000 deadweight tonnage (dwt) tanker. The results are caveated by stating that it is unclear how often the studied environmental conditions occur during voyages and that a specific route analysis should be undertaken with route optimisation expected to greatly improve the economics of wind propulsion methods.

This sentiment was echoed by Kukner et al. (2016) who stated that while instantaneous cost savings for kite propulsion may reach up to 50%, when considering wind conditions over a full route, reductions will be in the range of 10% - 35%. The authors applauded two main aspects of the kite when compared to other wind propulsion devices. Firstly, kite systems can be retrofitted to all existing cargo ships with far greater ease than other systems which rely on a mast type structure and, secondly, the systems work outside the turbulent boundary layer of the wind. Their operation at 150 m to 300 m above the ship deck allows for an undisturbed freestream flow and accounts for an extra 30% to 70% of available energy.

2.1.3. Flettner Rotor

Flettner rotors are rotating cylinders which use the Magnus Effect to produce a propulsive force from the wind (Copuroglu and Pesman, 2018). The Magnus effect is closely linked to the Bernoulli principle; the rotation causes higher

wind speed on the side which the cylinder is rotating towards, and lower wind speed on the opposite side. This results in a pressure differential and thus a lifting force develops (Searcy, 2017).

The German physicist Anton Flettner was the first to physically apply the concept to propulsion of ships. His 1926 crossing of the Atlantic on a craft powered solely by twin rotating cylinders cemented the concept as a viable propulsive option (Craft et al., 2014). This vessel, Buckau, is shown in Figure 2. Rapid development of diesel engines stalled further use of the Flettner rotor until it found reapplication in the carbon conscious environment of today. Currently there are multiple operating Flettner rotor ships with many more in early development. Norsepower offered the first commercially available retrofitting service. They deployed the Norsepower rotor sail on the Bore Ltd. owned M/S Estraden and reported fuel savings of 8% compared to the non-rotor configuration (Suominen, 2015).



Figure 2: Buckau - the first Flettner rotor ship (Craft et al., 2014)

Lu and Ringsberg (2020) have recently compared three ship wind-assisted ship propulsion technologies; their investigation studied the effect of the Flettner rotor, a wingsail and a DynaRig concept on oil tanker fuel savings for a set route. Their results show that the all three propulsion methods gave fuel savings of between 5.6% - 8.9% with the Flettner rotor giving the highest cost reduction for the smallest sail area. Following from these results a parametric study of the Flettner rotor was conducted in an attempt to analyse the sensitivity of fuel savings to rotor dimensions, rotor position and ship operation. It was found that higher spinning speeds and larger rotors were not always met with an increase in fuel savings - specific parameter combinations were optimal for different tested ships. Their work was concluded by highlighting the importance of a specific simulation model in pairing the appropriate shape and size of wind assisted propulsion method with ship type, speed, voyage routes and corresponding weather conditions.

Traut et al. (2014) compared numerical models for assessing the wind power input of a kite and a Flettner rotor

over five shipping routes. Advantages of the kite were highlighted in that it consumes very little space on the deck of a ship and it represents a cleaner, low carbon technology than the Flettner rotor - it does not require a consistently running motor during operation. The kite produced the highest single power contribution over the routes studied at 461 kW relative to the Flettner rotor at 373 kW. However the power variability of the kite was significantly greater in terms of both time and geographic location and it was noted that two or more Flettner rotors could produce a greater transient power. The study does not consider interaction effects between the propulsion technologies and the ship, an effect which may be reasonably predicted to negatively impact the Flettner rotor to a greater degree than the kite due to its closer proximity to the ship superstructure and hull. The study concludes that for fuel savings to be estimated, the implementation of these two technologies must be studied in regard to a particular vessel. Analysis should consider practical barriers to operation and the complex integration of power contributions between the wind propulsion device and the ship propeller. The work also noted that performance of the numerical setup could be further improved by including information on ocean currents along side wind data.

2.1.4. Actively Controlled Wingsails

Actively controlled wingsails are vertically mounted wing shape sections which use boundary layer control to improve lift over a wide angle of attack (aoa) range. The appearance is, in essence, a combination of the wingsail and the Flettner rotor — a vertical thick mast as seen with the Flettner rotor but maintaining an aerofoil type section as with the wingsail. Contrary to Flettner rotors, the active wing sail utilises blowing and/or suction to energise the boundary layer and the only movement of the physical system is to orient the aerofoil favourably with respect to the wind.

The first ship to utilise actively controlled wingsail technology was the Moulin à Vent, shown in Figure 3 (Charrier et al., 1985). This experimental ship was funded by the Cousteau foundation and confirmed previous wind tunnel tests on smaller scale models. Having demonstrated the feasibility of such a craft, development was started on a larger active wingsail propelled ship, the 30 m Alcione. This ship differed slightly from the Moulin à Vent in that it featured two aerofoils of reduced aspect ratio rather than one. This was to reduce storm wind loading which had eventually led to failure of the preceding ship.

With regard to modern wind propulsion literature, actively controlled wingsails represent a comparatively sparse area. Hcini et al. (2016) published a numerical method for predicting their aerodynamic performance. They confirmed their method with experiment and deemed their use of a vortex model as providing satisfactory representation of the performance characteristics of the active wingsail system. They concluded that the actively controlled wingsail offers a promising wind propulsion alternative but more experimental and theoretical results are required to prove its success.



Figure 3: The Moulin à Vent Charrier et al. (1985)

Guerra et al. (2016) performed numerical simulation of turbulent flow around an oval cross-section, active wingsail. Their geometry bears some resemblance to the actively controlled wingsail iteration tested in this work, however only employing suction rather than a blowing/suction combination. Their results show the suction increases lift to drag ratio and suppresses vortex shedding, eliminating vortex induced vibration.

To the knowledge of the authors, no studies perform a detailed comparison of actively controlled wingsails with their biggest competitor, the Flettner rotor.

2.2. Circulation Control

The Coanda effect was first investigated for aerodynamic use by Henri Marie Coanda in 1935. The phenomenon describes the ways in which the presence of external walls causes jet flows to attach, entrain and mix with surrounding fluids (Coanda, 1936). Viscous drag interaction between the fluid and the wall boundary acts to reduce the pressure on the wall side of the fluid and the resulting pressure gradient creates an unbalanced force acting to deflect the fluid in the direction of the contacting wall (Rodman et al., 1989).

For aerodynamic purposes the Coanda effect is used in three main situations (Reba, 1966). Firstly, a jet tangential to a curved surface tends to remain attached to that surface rather than continue in its original direction. Secondly, a free jet has the ability to attach itself to a close wall. Thirdly, jets flowing over curved surfaces by the Coanda effect tend to entrain more surrounding ambient fluid than that of straight wall enclosed jets, with some studies reporting up to 20 times increased entrainment by air volume (Rodman et al., 1989).

Conventional application of jet flow control to aerofoil design typically aims to delay flow separation and allow an aerofoil to produce a greater peak lift force before reaching stall. These uses are often limited to a small portion of the flight envelope and are not used continuously. Military applications where mission requirements dictate extremely short take-off or landing distances are prime examples of active flow control, where jets are utilised to increase the maximum lift coefficient and decrease the stall speed at the beginning and end of the flight. Other applications such as the Boeing 757 ecoDemonstrator craft which uses jet flow

control to delay rudder flow separation and maintain control authority in engine failure scenarios is another example of the specialised and particular cases in which jet flow control finds a beneficial real world application (Andino et al., 2019). Conversely, ship applications present a case for uninterrupted use of jet flow control. Any increases in mass presented by the inclusion of wings or fan components represent a very small fraction of the total mass of the craft. As well as this, since a component of the lift force is used for propulsive thrust, maintaining the flow separation delays and increased maximum lift coefficient is beneficial over the full operating time of the ship.

Zha et al. (2007a) proposed a now highly investigated method of circulation control, the co-flow jet (CFJ). Their method improved on conventional circulation control which had been predominantly used only during take off and landing and instead presented a concept with application to the whole flight. The CFJ mechanism employs a high energy leading edge jet which attaches and travels along the majority of the upper surface. The jet injection works in tandem with a suction slot near the trailing edge which recirculates equal mass flow back to the injection slot. This recirculation of air is important to the overall efficiency; some kinetic energy is recovered by using the high energy jet flow near the suction slot as the jet source. This is in contrast to circulation control systems which employ an injection jet only; the jet flow in this case is the result of accelerating low energy freestream flow, requiring an increased energy input. Positioning the suction duct in-line with the fast moving jet flow results in a greater initial velocity and the additional kinetic energy required to reach the jet velocity is less. The positioning of the jet and suction slots is also noted in the CFJ introductory study as helping increase efficiency over standard jet and blown flap type circulation control systems. The CFJ jet slot is positioned near the leading edge, in a region of low pressure, and the suction slot near the trailing edge, in a relatively high pressure region again aiding in the energy requirements for circulation.

The work makes use of a common method of quantifying the extent of the jet flow, using the jet momentum coefficient, C_{μ} , as a measure of the momentum of the jet relative to the main flow. This is defined as:

$$C_{\mu} = \frac{\dot{m}_J V_J}{\frac{1}{2} S \rho_{\infty} V_{\infty}^2} \quad (1)$$

where, \dot{m} is the jet injection mass flow rate, V_J is the jet velocity, S is the wing area, ρ_{∞} is the freestream air density and V_{∞} is the freestream air velocity.

The results found that a NACA2415 aerofoil employing the coflow jet system was met with a significantly increased lift as well as greatly reduced drag, including negative drag at certain aoa due to the CFJ mechanism of filling the wake and generating a negative pressure drag greater than skin friction. The mechanism for these improvements was stated as the existence of strong turbulent mixing and diffusion between the jet and the main flow.

Table 1
Model readiness rating

Turbulence Model	MRR Level
SA	4
SST-V	3
SSG/LRR-RSM-x2012	3
Wilcox2006-klim	2
L-kL-MEAH2015	2

3. Computational Set-up and Validation

The design methodology of the actively controlled wing-sail studied here follows from that of Zha et al. (2007b). The system uses a coflow jet type combination of blowing and suction to energise the boundary layer, transporting energy to the inner part of the shear layer and allowing the main flow to overcome the severe adverse pressure gradient. This circulation control mechanism allows the wing to maintain attached flow up to much higher angles of attack than usually possible and, in certain situations, allows high lift values with a small or negative drag penalty. Differences exist between the two systems in that Zha et al. explicitly state that the CFJ aerofoil does not use the Coanda effect at the leading and trailing edges but instead the jet path only follows a portion of the upper surface. This contrasts with the jet inlet point and large radius of the SWAP geometry which has a jet opening on the lower surface, so that the Coanda effect occurs around the leading edge and onto the upper surface. However the similarities are enough to merit the use of the Zha et al. (2007b) CFJ aerofoil wind tunnel data as experimental validation for the CFD model used here.

3.1. Co-flow jet validation case

The NASA Langley Research Center has published verification information for a 2D coflowing jet case. The data they provide is not intended to establish the ‘goodness’ of a model for a comparison with a specific experiment but rather to ensure that a selected model has been implemented correctly (Rumsey, 2020).

NASA has also classified several models under their model readiness rating (MRR) system for such applications. Their work evaluated five turbulence models, the Spalart-Allmaras model, the Menter Shear Stress Transport model with vorticity source term, the full second-moment Reynolds stress model, the Wilcox k- ω model and the 2015 version of the k-kL model. This rating system attempts to quantify how well-used and tested a model is rather than judging the quality or capability of turbulence models Rumsey (2016). Based upon this criteria, the Spalart-Allmaras model performed best out of the tested models. This information is listed in Table 1.

As mentioned above, the work of Zha et al. looks at the effects of combined blowing and suction on a coflow jet (CFJ) modified NACA0025 section. The modified aerofoil follows their CFJ naming convention, where the jet and suction widths are defined as a percentage of chord. CFJ0025-065-196 refers to the NACA0025 aerofoil with a

jet injection width and suction width of 0.65% and 1.96% chord respectively. The simulations were two-dimensional with a chord length of 0.1527 m. The upper surface was translated downwards to meet the jet and suction faces. The jet and suction faces are located at 7.11% and 83.18% of the aerofoil chord. The geometry is shown in Figure 4. The highlighted surface is a faux surface added to give finer control over the mesh density along the blown upper surface. This helps to accurately capture the flow field in a region of high gradients which has a significant effect on the aerofoil performance characteristics.

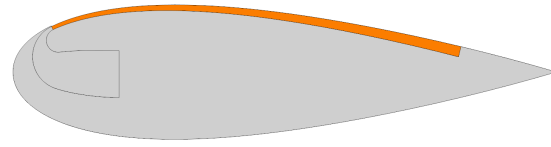


Figure 4: CFJ0025-065-196 geometry

The jet cavity has been included in the simulation to allow the jet flow to develop and remove any non physical velocity gradients between the jet boundary condition and the aerofoil upper surface. This also allows space for the jet flow to develop and then to fully capture the turbulent mixing and energy transfer between the jet and main flow. The jet cavity and fine upper surface mesh control is shown in Figure 5.

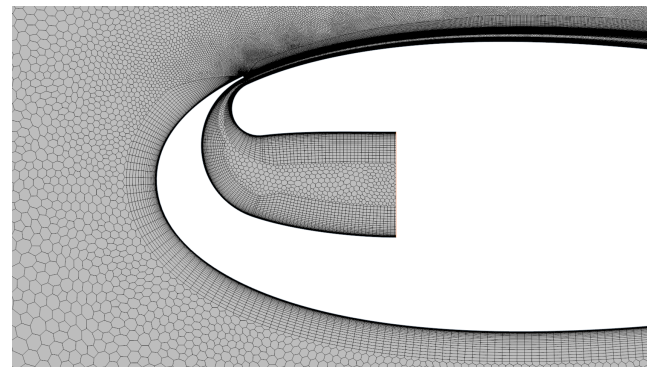


Figure 5: Cavity and artificial jet surface mesh

The mesh continuum followed the best practice guidelines for external aerodynamics published by Siemens relating directly to Star-CCM+ (Ewing, 2015). Mesh spacing over the upper surface was set to 0.1% chord with at least 5 divisions for all lips and the trailing edge. Lower aerofoil surface spacing was set to 0.5% chord and a value of 1.05 used for the growth rate between cells. The mesh was controlled by the Star-CCM+ 2D automatic mesher using the

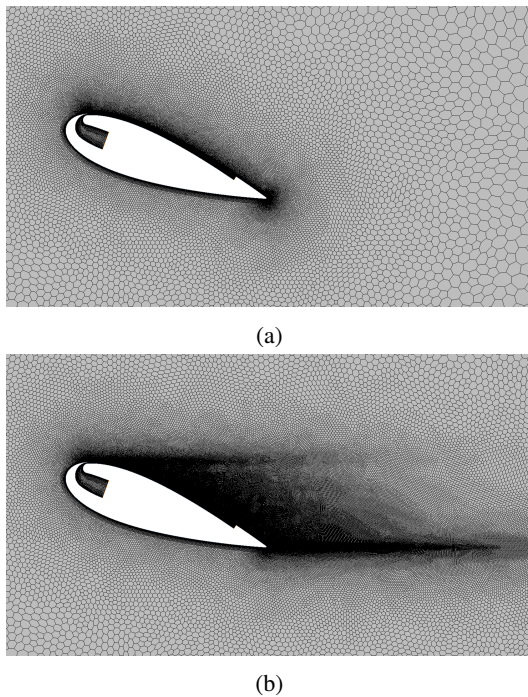


Figure 6: (a) Base mesh (b) Adaptive refinement

polygonal cell and prism layer models - the latter used to capture the boundary layer region adjacent to the surface. Prism layers extend well into the domain as a method of accurately capturing the interaction and entrainment of the high momentum jet with surrounding air. The y^+ values are less than 1 on wall boundaries for all cases.

Adaptive mesh refinement was included in the simulation determined by a custom function based on the gradients of velocity magnitude. Accurate error estimation for adapted grids is difficult to obtain. It was therefore assumed that the greatest error occurs in the high-gradient regions of the flow and the already available physical flow features may be used to dictate grid adaptation. Additional isotropic wake refinement was added, reducing cells to 25% of base value extending 3 chord lengths from the upper and lower surfaces. The influence of these additional refinement parameters is shown in Figure 6.

The velocity magnitude gradients were modified by cell area and cells pertaining to the largest 15% of values had their cell size reduced by a factor of 10.

The wind tunnel dimensions and therefore the information about the experimental blockage ratio was not included with the data of Zha et al. Although blockage considerations may affect the conclusions drawn in Section 3.6, the influence of boundary walls was not considered in the CFD simulations. A rectangular domain was used and extended 20 chord lengths upstream and in positive and negative y , and 40 chord lengths downstream.

The cell count was approximately 300,000 for each run. An increase in the mesh cell count from 200,000 to 300,000 was met with a change in lift coefficient of 0.4% for a nominal case. The results were deemed suitably converged

Table 2
Physics Continuum Selection

Model type	Model Selected
Dimensions	2D
Time	Steady
Flow	Segregated Flow
Equation of State	Constant Density
Viscous Regime	Turbulent

and the denser mesh used simply because its computational requirements could be satisfied comfortably within the physical time allocated to this section of the project. Mesh density was varied by changing the mesh base size, effectively scaling without the need for alteration of the adaptive and wake refinement controls.

3.2. Boundary Conditions

As per the work of Zha et al., the total pressure at the jet inlet boundary was iterated until the jet momentum coefficient, C_{μ} , matched the experimental reading. The jet momentum coefficient values are only provided up to a maximum angle of attack of 45° after which point values can be estimated but not confirmed to be exactly as experiment.

The domain inlet boundary total pressure was set to replicate the experimental Reynolds number of 380,000. This resulted in an approximate inlet velocity of 33 m/s .

An iterative static pressure boundary condition was set on the suction outlet. The pressure value was set to match the jet injection mass flow rate and ensure there was no additional mass added to the domain.

3.3. Solver Settings

The low speed, incompressible tests made use of a segregated approach in solving the flow equations for mass and momentum. The physics continuum models are shown in Table 2. The finite volume method is used for discretization of the governing equations with the SIMPLE algorithm being used for coupling of pressure and velocity.

Grid Sequencing Initialization (GSI) was used to generate higher quality initial solutions by using an implicit, incomplete-Newton algorithm to approximate a first order, Euler flow field on levels of coarsened meshes (Shankara and Snyder, 2012). Second order upwind spatial discretization was used for the convection terms, and the second-order order central discretization for diffusion.

3.4. Governing Equations

3.4.1. Spalart-Allmaras

The Spalart-Allmaras (SA) turbulence model is a one equation model which determines the turbulent eddy viscosity by solving a transport equation for the modified diffusivity in order to determine the turbulent eddy viscosity (Spalart and Allmaras, 1992). This model was applied in its standard, low Reynolds formulation using a y^+ value no greater than 1 over all wall surfaces. The empirical curvature correction approach of Spalart and Shur (SARC) has been applied to

more accurately capture the large streamline curvature due to jet attachment (Shur et al., 2000).

3.4.2. *k*- Ω -SST

A well-documented shortcoming of standard eddy viscosity models is poor prediction for flows exhibiting anisotropic turbulence such as with strong curvature or stress driven secondary flows (Siemens, 2018). As a means of investigating the influence of these effects for the studied geometry, comparisons are made with a more advanced model – *k*- ω -SST. As a modification to the Standard *k*- ω model, Menter proposed the shear stress transport model (SST) which acts to use a blending function to favour a *k*- ϵ type model near the farfield boundaries and a *k*- ω model near the walls (Menter et al., 2003). One further modification to this model is again the inclusion of curvature correction parameters which alter the turbulent kinetic energy production term according to the local effects of rotation and vorticity (Smirnov and Menter, 2009). This modification is commonly known as SST-CC.

3.5. Convergence Criteria

Asymptotic solution monitors were placed on the lift coefficient, drag coefficient, pressure drop, jet inlet mass flow and suction outlet mass flow. The convergence criteria were satisfied when the normalised change in these values fell below 1×10^{-5} over 5 iterations. The pressure drop was defined as the change in total pressure between the recessed jet inlet boundary and the suction outlet boundary. Additional monitors were placed on the residuals for relevant flow variables

3.6. Model Selection

The comparison between the Spalart-Allmaras turbulence model, the *k*- ω -SST turbulence model and the experimental lift data of Zha et al. is shown in Figure 7.

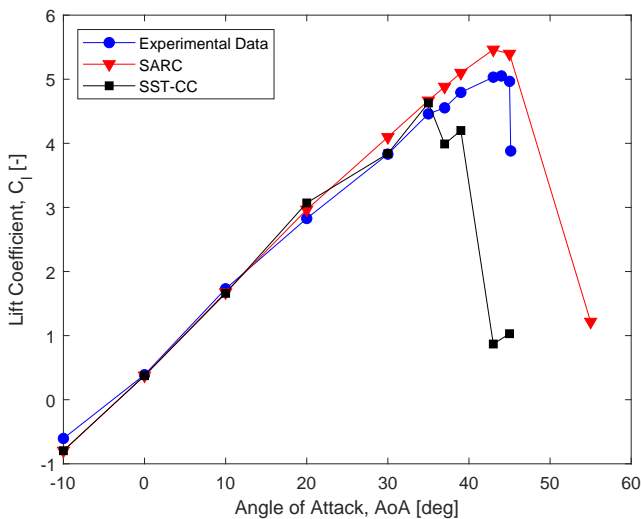


Figure 7: CFD comparison with experimental data

Both models predicted lift well for most of the angle sweep. The SST-CC model predicted stall too early and was met with an abrupt and exaggerated drop off in lift coefficient approaching the experimental stall region. The SARC model over-predicted the maximum lift coefficient by 8.1% and the stall onset occurred approximately 5° later than experiment. The SST-CC model underpredicted maximum lift coefficient by 8.3% and the stall onset was approximately 8° earlier in the angle sweep.

Overall both models performed well, with the Spalart-Allmaras model being chosen for simulations going forward due to its strong performance for circulation control flows in the literature and its good performance over the validation case. The SARC simulations also exhibited much less computational instability – especially in the regions near stall and with separated flow.

Yaras and Grosvenor (2002) have found previously that, when considering a combination of consistent prediction accuracy, robustness and computational efficiency, the Spalart-Allmaras model was preferred over SST for separated flows and flows exhibiting high streamline curvature. Bardina et al. (1997) have also found similar conclusions when comparing the SA and *k*- ω -SST models for a variety of simple free shear and complex separated jet flows. The SA model performed best in terms of numerical performance and in predicting mixing layer flows. The SA and SST models outperformed all other models tested, although it was noted that there is still considerable room for improvement.

When considering that the parametric design optimisation for a SWAP wing on board a ship deck considers a very wide angle of attack sweep – and therefore many regions of strongly separated flow – this improved stability is extremely valuable. Furthermore, as a one equation model, it offers a reduction in the required computational resources relative to classification of turbulence by *k*- ω -SST.

4. Design Optimisation and Results

4.1. Surrogate Approach

Having established an accurate high fidelity flow simulation, a routine was developed which integrates this CFD methodology with the SWAP geometry and with a Kriging model and a genetic algorithm for optimisation.

A surrogate based approach is very useful to solve optimisation problems where the performance to be optimised can only be determined by computationally expensive simulations. The surrogate model, or meta-model, learns the coupled input-output information obtained by sampling the expensive function(s) in a limited amount of sampling points, and is able to generalize the learned information to all points of the search space (Forrester et al., 2008).

Computational fluid dynamics is an area particularly suited to surrogate modelling with an extensive array of proven applications (Paiva et al., 2010). Obtaining functional outputs for a given input vector for complex, real world flows requires the use of computationally intensive CFD simulations to evaluate new designs. The large data

collection time associated with such methods means that an iterative optimisation process cannot be realistically applied without the introduction of a low evaluation cost, surrogate model.

Section 4.3 makes use of Kriging models to interpolate performance metrics based upon a known set of design variables. Kriging models treat the experimental response as if it were the realisation of a stochastic process, a method which initially seems unsuited for predicting the output of deterministic computer code but has demonstrated wide ranging success in CFD approximation and specific application to complex optimisation problems involving ships (Park et al., 2006) (Lee et al., 2016). The unknown objective function is expressed as a combination of a linear regression model and deviations such that:

$$y(X) = \mu + Z(X) \quad (2)$$

where X is the n dimensional input vector (in this case a wing geometry vector defined in 4.2), μ is a constant global model and $Z(X)$ denotes a local departure from the global model (Zou et al., 2013).

The covariance of matrix $Z(X)$ is given by

$$\text{cov}(Z(X^{(i)}), Z(X^{(j)})) = \sigma M[R(X^{(i)}, X^{(j)})] \quad (3)$$

where $R(X^{(i)}, X^{(j)})$ represents the correlation function. For all cases the Gaussian correlation function was used meaning that

$$[R(X^{(i)}, X^{(j)})] = \exp(-\theta \sum_{k=1}^d |x_k^i - x_k^j|^2) \quad (4)$$

This correlation has been shown to produce a smooth and infinitely differentiable function suitable for capturing model trends without over-fitting to input data (Park et al., 2006).

For all Kriging implementations the Design and Analysis of Computer Experiments (DACE) MatLab toolbox was used. This is a freely available toolbox with several Kriging implementations allowing for fast and simple model creation (Lophaven et al., 2002).

4.2. Design variables

The aerofoil outer surface is unquestionably important in influencing the device's aerodynamic characteristics, however there are many other factors that determine performance for circulation control aerofoils. Parameters such as jet outlet width and suction inlet width have strong effects on the Coanda jet and control the extent of mixing between the blown air and the freestream. Further parameters such as the jet exit location also influence this relationship and have a complex and non-linear interaction with performance metrics.

It is a well-documented rule in surrogate modelling that as the number of design variables increases, the computational requirements of the optimisation increase, and more iterations are required to reach the acceptable level of

convergence. If the total number of design parameters for the SWAP device are to be kept within a manageable range while retaining the important circulation parameters, concessions are required in parametrisation of the outer aerofoil surface. The NACA modified 4-digit method was selected for shape definition.

For the SWAP device to be used over a wide range of wind directions and two-way routes, the aerofoil must represent symmetric geometry. Use of the 4-digit NACA system allows creation of a symmetric aerofoil with only one initial parameter - the thickness to chord ratio - and two additional parameters added in the modified variation which define the position of maximum thickness and the sharpness of the leading edge. The outer surface curves were produced using the naca456 program made available by Public Domain Aeronautical Software (Carmichael, 2001).

One geometric constraint exists to ensure that the flap rotation point is placed further aft than the position of the suction slot. Figure 8 gives a representative geometry showing seven design variables that, in conjunction with the leading edge radius, describe a SWAP wing. This setup allows the jet location to be controlled by the Jet Angle parameter. The greater the Jet Angle, the further along the chord the jet opening will be. The suction location is controlled by the Rotation Point and Flap X parameters. Since the suction slot is located at the beginning of the tail, these two parameters define where the tail begins and how it is orientated with respect to the chord line.

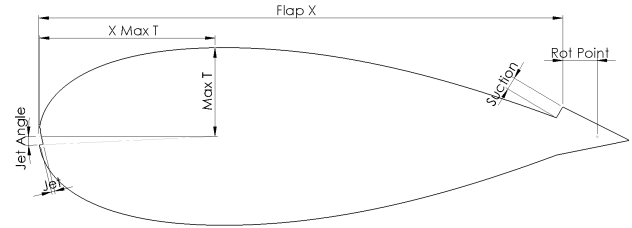


Figure 8: SWAP geometry design variables

Certain combinations of design variables resulted in geometries which could not be constructed. For these cases the parameters defining the leading edge and jet opening led to a situation in which it was impossible for a single curve with no inflection points to join the jet opening to the main aerofoil body. The join would instead curve back on itself and result in either infeasible geometry or a curvature situation which would strongly disrupt the Coanda jet attachment of the leading edge. These situations are given a large penalty in the optimisation objective function as a method of steering the algorithm away from such cases.

Over the course of the optimisation routine, the algorithm occasionally experienced combinations of geometry, α and $C\mu$ which resulted in an unsteady flowfield. Typically, these cases existed where the jet momentum coefficient was not high enough to overcome the adverse pressure gradient and create fully attached flow. Due to the work

considering an automated optimisation routine, it was not computationally possible to consider unsteady solver methods for these individual cases. However, it was also felt that eliminating these cases from the optimisation did not fully make use of the data. As a rule, the unsteady cases exhibited lower lift and higher drag than the simulations which produced fully attached flow, and therefore were used as drivers to push the optimisation algorithm away from these areas. When simulations were not fully converged and oscillations were observed in force reports, the minimum of the oscillating lift value and maximum of the oscillating pressure drop was used as the objective value. By doing this there exists a natural penalty function which penalised the unconverged, unsteady or stalled CFD simulations while still giving the optimisation algorithm information about the parameter combinations and areas of the domain that should be avoided.

4.3. Initial Sampling and Robust Formulation

An even distribution of input variables is required in order to capture global trends in the design space and ensure the domain is evenly explored. As a method of sampling the design space, Latin hypercube sampling (LHS) was employed in order to populate an initial 30 by 8 design array. LHS is a type of stratified Monte Carlo sampling which divides design variable ranges into intervals of equal probability (Keramat and Kielbasa, 1997). One value from each interval is selected and randomly combined with values from intervals relating to the other parameters. Thirty initial sample points is small for an eight-dimensional design problem but was the maximum available computationally due to each wing geometry requiring multiple simulations to define its performance over a range of wind conditions.

An actively controlled wing sail in situation on board a large bulk carrier will see a very wide range of wind speeds and flow angles. The geometry optimisation must therefore consider a range of design conditions and ensure that the aerofoil performs consistently with no sharp performance drops or stalls due to expected changes in environmental conditions.

Ju and Zhang (2012) found good results when using meta-models to optimise wind turbine geometry across varying wind environments. Their use of an artificial neural network to quantify lift and drag coefficient was met with errors of less than 0.1% for their specific case and dramatically reduced the computational resources required to complete the robust optimisation problem. A similar process is proposed here.

This method simulates each geometry over a small set of α and C_{μ} values and then attempts to extrapolate the information and gain a more complete picture of the aerofoil performance over the full α and C_{μ} range. For each geometry, a second 30 point Latin hypercube is used, this time representing a distribution of α and C_{μ} values. This is optimised using the minimax criterion over 1000 iterations. The α and C_{μ} values to be simulated for each geometry are bounded by $[0\ 90]$ and $[0\ 1.5]$ respectively. The

distribution of values is shown in Figure 9. Each point in the hypercube represents the CFD input conditions for each studied geometry.

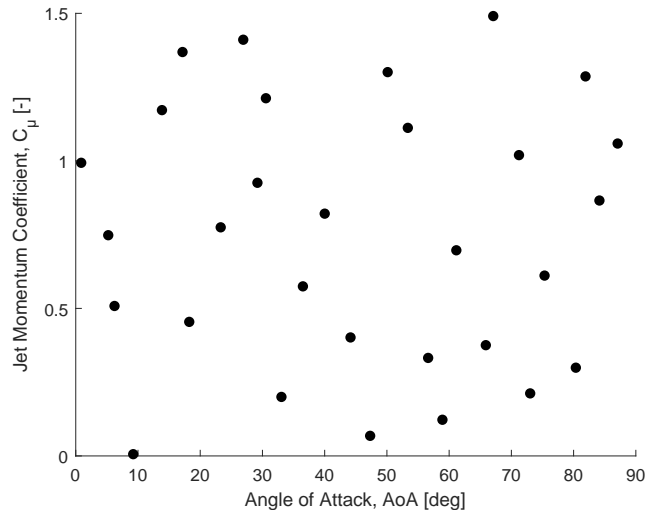


Figure 9: Latin hypercube distribution of α and C_{μ} for CFD simulation

Figure 10 and Figure 11 plot the lift against angle of attack for the baseline aerofoil, firstly using data collected solely from CFD evaluations and then from a trained Kriging meta-model. The full evaluation consists of 84 CFD simulations, one corresponding to each data mark. Figure 11 however shows data extracted from the Kriging meta-model as used in the optimisation. The underlying model was trained using 30 CFD simulations with input conditions dictated by the Latin hypercube of Figure 9. The data is then extrapolated to cover the full range of parameters.

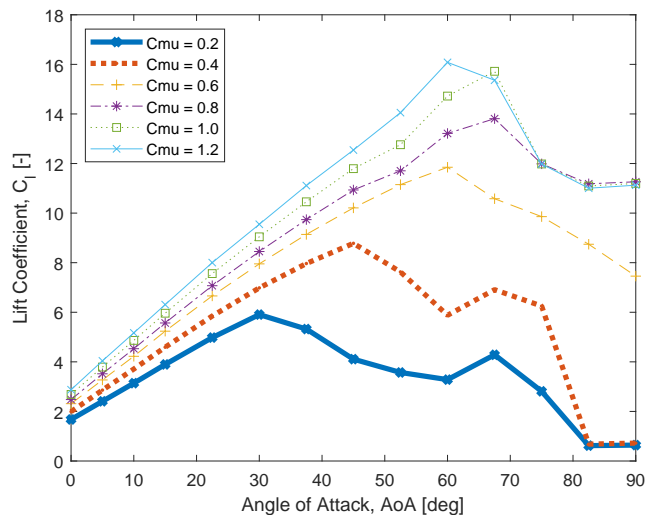


Figure 10: Baseline geometry C_l vs α trends using direct data from 84 CFD simulations

Trends are mapped well between the two methods with only slight discrepancies between magnitude and position of maximum C_l . When considering that the meta-model method requires one third the required CFD simulations,

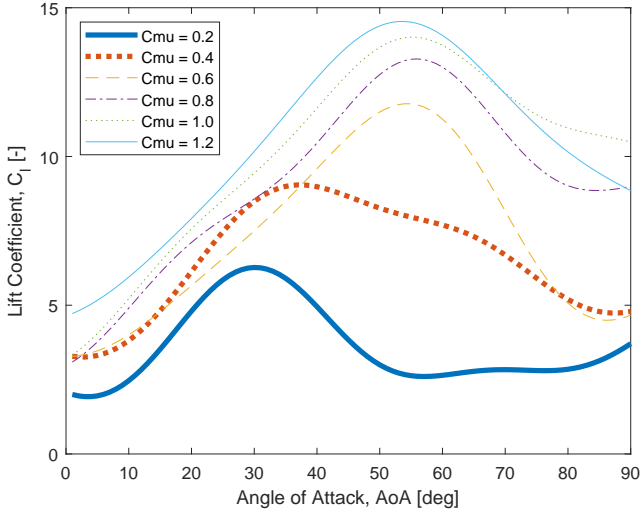


Figure 11: Baseline geometry C_l vs AoA trends mapped using a Kriging model trained on 30 CFD simulations

the process was deemed to offer a suitable balance between performance and computational resources. Using the meta-model method to evaluate the performance of each of the 30 initial sample geometries required 900 CFD simulations in total. CFD results were obtained using the ARCHIE-WeSt High Performance Computer based at the University of Strathclyde.

Figure 12 gives a clearer picture of the trend mapping by showing the lift against angle of attack for the baseline aerofoil at $C_\mu = 0.2$. The direct CFD sweep consists of 12 CFD simulations compared to the data from the trained Kriging model. While the direct CFD sweep method would require 12 or more additional simulations in order to quantify performance at a different C_μ value, the Kriging method uses the same 30 point data set to quantify all combinations of C_μ and aoa.

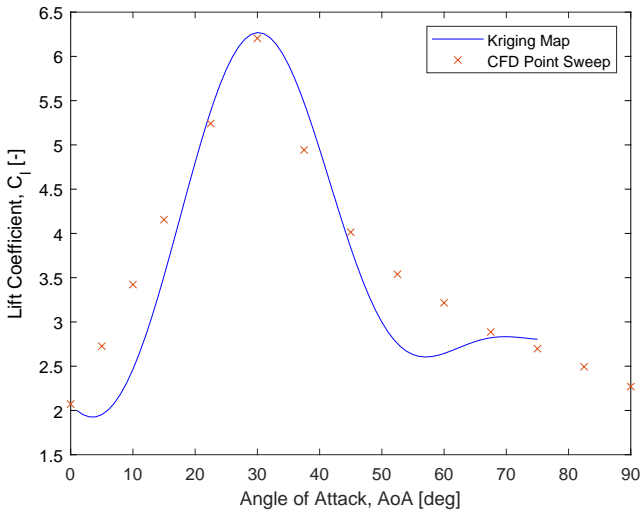


Figure 12: Lift coefficient vs AoA trend of a trained Kriging model plotted against direct CFD data. Jet momentum coefficient = 0.2

4.4. Objective Function

The optimisation being considered is a single-objective, multi-point optimisation aimed at maximising the lift coefficient for a fixed amount of energy input. This energy input takes the form of a fixed fan power that is available on board the ship to operate the aerofoil circulation.

With the lift coefficient of a circulation control aerofoil being linked with the blowing momentum coefficient and with this in turn being linked to the pressure difference between the suction and blowing slots, further use of the Kriging meta-models is required to define the fan power required for each geometry across a wide range of aoa and C_μ values. The volumetric flow rate through the fan is defined as,

$$Q = \frac{\dot{m}b}{\rho} \quad (5)$$

where \dot{m} is the two-dimensional mass flow rate through the fan, b is the wingspan and ρ is the air density.

Substituting the standard definition for jet momentum coefficient as seen in Equation 1 in place of the circulation mass flow gives,

$$Q = \frac{2SV_\infty^2 C_\mu b}{V_J} \quad (6)$$

The power required is then,

$$P_{req} = Q\Delta p = \frac{2SV_\infty^2 C_\mu b\Delta p}{V_J} \quad (7)$$

Where, Δp is the pressure drop across the fan as defined by the Kriging meta-model. By equating the required fan power with the available fan power, the maximum volumetric flow rate achievable by the fan is found. This is then used to define the maximum jet momentum coefficient attainable for each angle of attack.

Plotting the crossover points between the power required and the available fan power results in Figure 13 which shows how the maximum C_μ value varies with aoa for the baseline aerofoil. This data exhibits a non-monotonic trend which arises due to the local pressure conditions on the upper surface as the angle of attack increases. While the flow remains attached, increasing the angle of attack acts to create a larger negative pressure on the aerofoil leading edge close to the jet exit point. This has the effect of decreasing the pressure drop and increasing the maximum achievable jet momentum coefficient. As the angle of attack continues to increase and the flow begins to detach, the pressure differential between the jet and suction slots begins to change depending on the constant pressure in the separation region which now encompasses the suction slot, and on the magnitude of the natural penalty discussed in Section 4.2.

This array of maximum C_μ values attainable at each aoa acts as an input to the previously defined lift coefficient

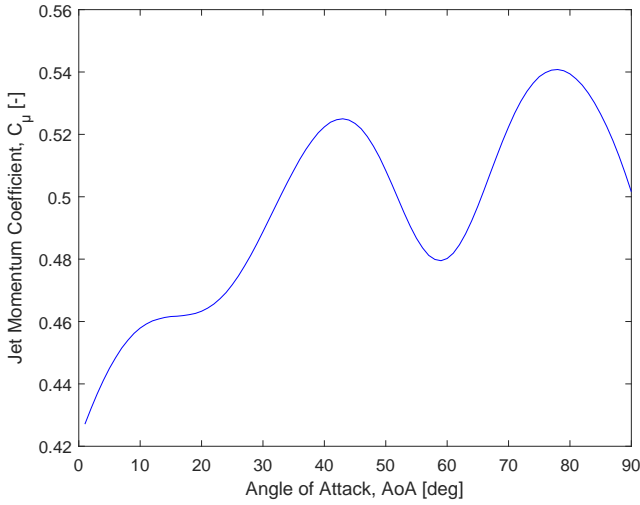


Figure 13: Max C_{μ} possible at each angle of attack for the baseline aerofoil

Kriging model. The maximum possible lift coefficient for the given fan can then be found at different circulation conditions and wind environments. Since the jet momentum coefficient is a measure of the momentum of the jet relative to the main flow, variations in freestream velocity are met with changes in the jet mass flow and the pressure drop for fixed C_{μ} . This allows for evaluation of each geometry at freestream velocities differing from the 10 m/s set in the CFD simulations without the need for multiple simulations at the same C_{μ} values for different wind speeds. The studied Reynolds number covers the range 2 - 3 million. While there will be some influence of the Reynolds number on the stall angle and overall lift vs angle of attack relationship, at this Reynolds number range it is thought to not significantly alter the results.

The pressure drop in Equation 7 for design points differing from the freestream velocity of the CFD simulations is modified as below,

$$\Delta p = \left(\frac{V_{\infty}}{V_{\infty ref}} \right)^2 \quad (8)$$

where $V_{\infty ref}$ is the 10 m/s freestream velocity of the CFD simulations and V_{∞} is the freestream velocity for off-design points.

Figure 14 shows how the lift coefficient of the baseline aerofoil varies with aoa at various wind speeds. The trend is for lower wind speeds to be met with increased lift coefficients due to the fixed available fan power being able to achieve greater C_{μ} values at lower freestream velocities. Note these graphs differ greatly from a standard aerofoil lift coefficient variation for circulation control aerofoils since each angle of attack corresponds to a different jet momentum coefficient as has been shown in Figure 13.

The optimisation is presented as a multi-point optimisation considering a weighted average over multiple wind speeds. Weights were set equally based on three expected

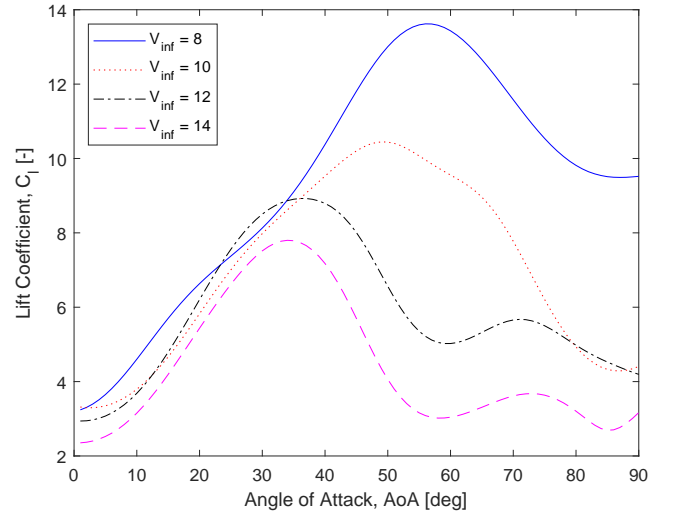


Figure 14: Variation of jet modified C_l with aoa for the baseline aerofoil at different free stream velocities

wind speeds, 8 m/s, 10 m/s and 12 m/s. This allows for selection of a geometry which gives consideration to off-design points, ensuring there are no sharp thrust decreases due to variations in wind speed.

The final objective function is shown in Equation 9 representing an equally weighted average of the percentage change in lift coefficient relative to the baseline aerofoil for N different wind speeds.

$$f(x) = \frac{1}{N} \sum_i \frac{Cl_{max}(V_{\infty}(N), x) - Cl_{max}(V_{\infty}(N), x_0)}{Cl_{max}(V_{\infty}(N), x_0)} \quad (9)$$

where Cl_{max} is the maximum lift coefficient of the wing, $V_{\infty}(N)$ is the freestream velocity for the N th objective point and x is a vector representing the geometric parameters of the aerofoil with x_0 pertaining to the baseline case.

After a geometry has been assigned an objective function value, this data now acts as the basis for a third and final regression model. A vector describing the 8 geometric variables of a SWAP wing is mapped against this lift coefficient percentage increase. Having trained this final model, it can now be optimised using iterative methods at low computational cost using the genetic algorithm.

The optimal point referring to a new wing geometry is then automatically constructed in Solidworks and simulated across the 30 combinations of aoa and C_{μ} in Star-CCM+. The new data is added to the model, improving its fit to the underlying black box objective function and moving the optimal point before the process is repeated. A flow chart illustrating the optimisation process is given in Figure 15.

4.5. Resulting Geometry

The optimisation routine terminated after 18 geometry iterations resulting from 540 CFD simulations. Figure 16 shows the normalised variation in design variables as the optimisation routine progressed.

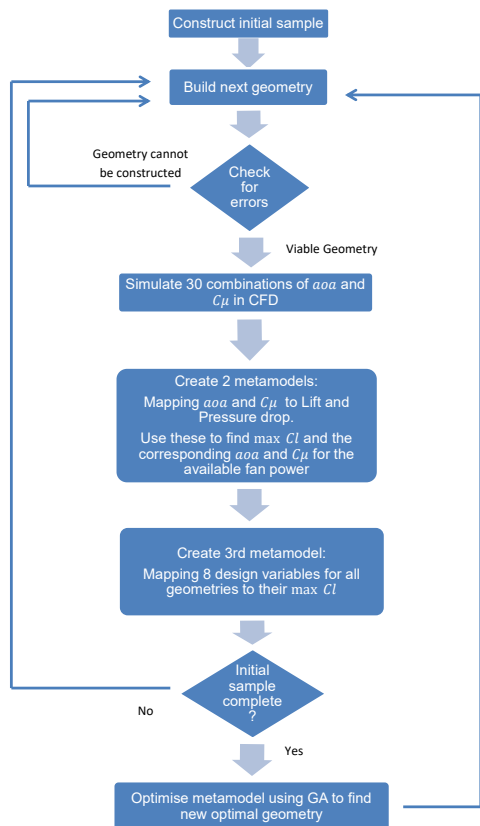


Figure 15: Optimisation flow chart

A representative image showing the percentage variations between the optimised and baseline geometries is shown in Figure 17.

The objective function value for the optimised aerofoil shape was 13.17, representing an average percentage increase in maximum lift coefficient of 13.17% for a circulation control wing operating at 8-12 m/s freestream velocity. The percentage increases in maximum lift coefficient for each wind speed is given in Table 3.

Table 3

Percentage increases in maximum Cl relative to the baseline aerofoil at different wind speeds

Velocity (m/s)	Max Cl % change relative to baseline
8	15.05
10	15.67
12	8.78

As a means of ensuring that the Kriging model trained upon the 30 point Latin hypercube had accurately modelled both the trends and exact lift values, the optimised geometry was simulated over a very wide range of aoa and C_{μ} values in CFD. The variation of lift coefficient and pressure drop with aoa is given in Figure 18 and Figure 19 for both the baseline and optimised aerofoil geometry at a blowing

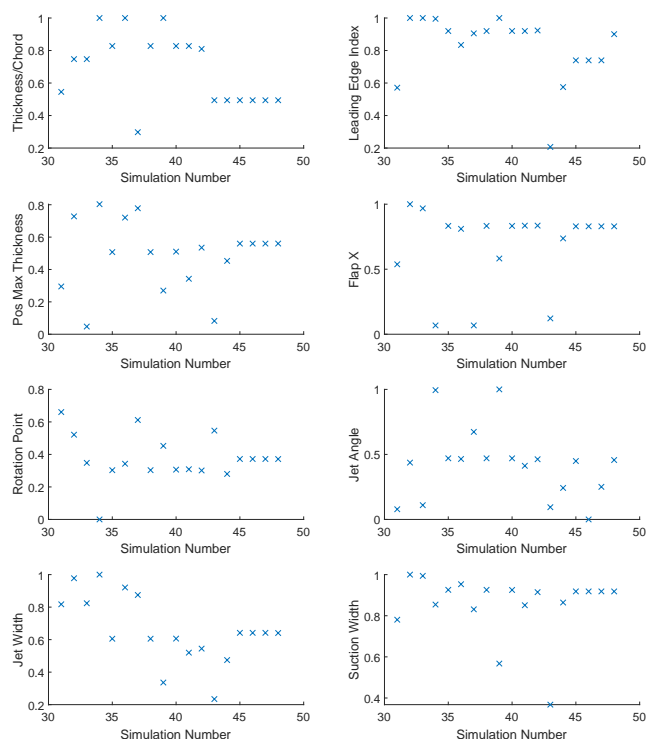


Figure 16: Normalised progression of design variables

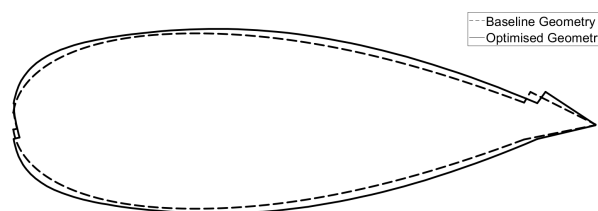


Figure 17: Representative geometries of the optimised and baseline aerofoils

momentum coefficient of 0.4. All parameters shown in Equation 1 were consistent meaning that the circulation mass flow is the same between simulations. While the maximum lift coefficient in Figure 18 is approximately equal between the baseline and optimised aerofoil, the pressure drop between the jet inlet and the suction outlet was much higher for the baseline case. This means that the optimised aerofoil can achieve a larger C_{μ} value for the same circulation fan power and, with more momentum being transferred to the inner part of the shear layer, the potential achievable lift is greater.

Figure 20 through Figure 22 show the variations of pressure drop and lift with angle of attack when factoring in the available fan power at the three tested wind speeds.

As has been shown, the main driver of the increase in lift was the reduction in the pressure drop between the jet and suction faces. This allowed for a higher C_{μ} value to be reached across all angles of attack relative to the baseline aerofoil. The results show a clear trend of dramatically decreasing the required pressure drop while maintaining similar trends with angle of attack for both pressure drop and

Wind Ship Propulsion Optimisation

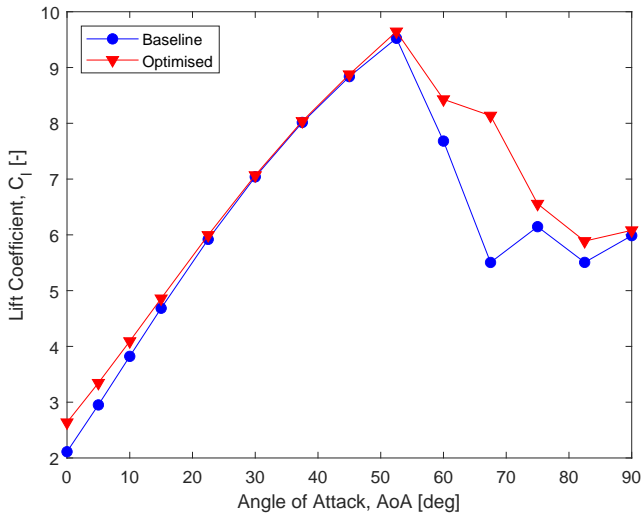


Figure 18: Variation in C_l with α for the baseline and optimised geometries at a C_μ value of 0.4.

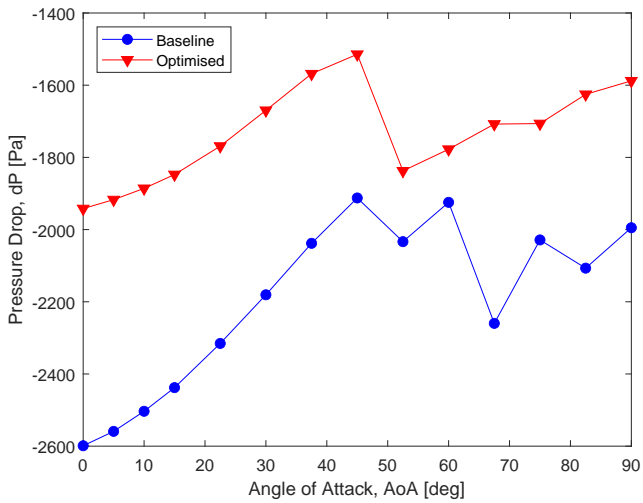


Figure 19: Variation in Pressure drop with α for the baseline and optimised geometries at a C_μ value of 0.4.

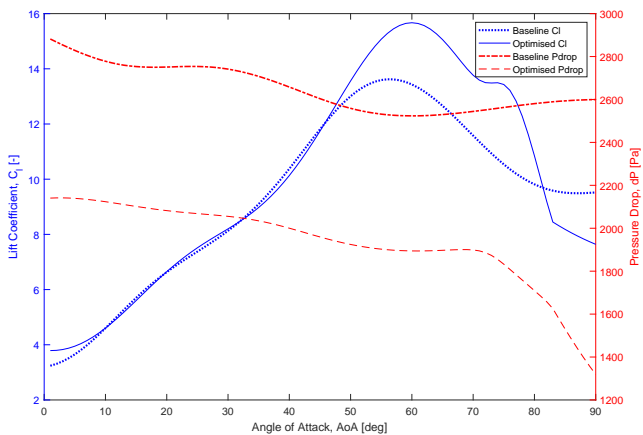


Figure 20: Variation of C_l and Pressure Drop with α at 8m/s freestream velocity

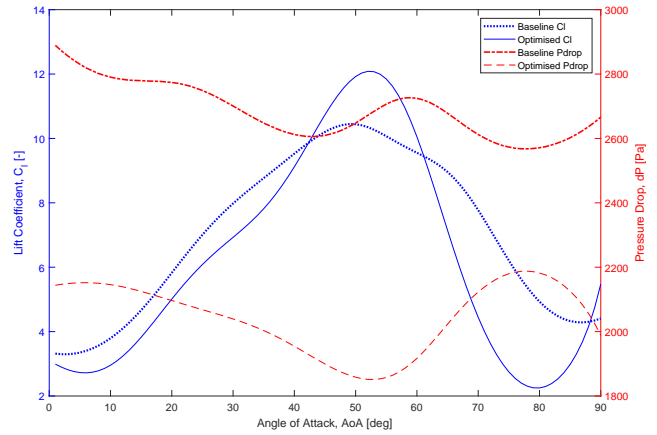


Figure 21: Variation of C_l and Pressure Drop with α at 10m/s freestream velocity

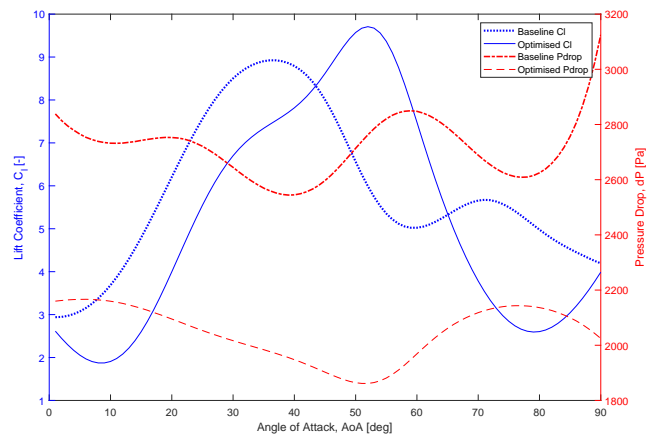


Figure 22: Variation of C_l and Pressure Drop with α at 12m/s freestream velocity

lift coefficient. This effectively allows the same additional momentum to be added to the domain by the circulation control system for a reduced pressure drop cost. Figure 24 shows the flowfield around the trailing edge of the optimised aerofoil at a C_μ value of 0.4, illustrating attached flow at 30 degrees angle of attack. Streamlines show the jet flow acting to produce circulation conditions consistent with the Kutta condition at the trailing edge. Pressure coefficient distributions are provided for both a high and low circulation momentum case in Figure 23. The lift force augmentation due to increasing the circulation momentum is clear to see, with a much increased negative pressure over the aerofoil upper surface.

The ability of this circulation setup to produce very low, occasionally negative drag coefficients in attached flow scenarios is observed in the wake. The usual low momentum wake region is replaced by high momentum fluid from the jet flow. Figure 25 shows a total pressure coefficient traverse five chord lengths downstream of the aerofoil for a range of jet momentum coefficients. The low blowing momentum case shows a somewhat standard viscous wake profile with a total pressure coefficient of 1 at the extremes and a reduced region

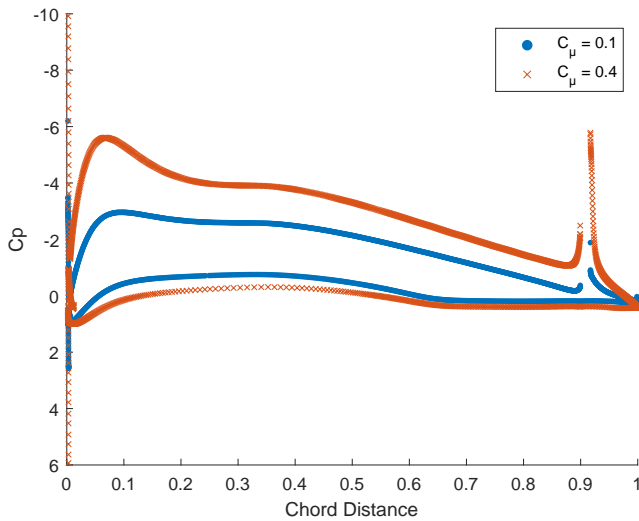


Figure 23: Variation of pressure coefficient at C_{μ} values of 0.1 and 0.4, $\alpha_{oa} = 0^{\circ}$

downstream of the aerofoil. As the circulation momentum increases, the higher mixing effect and increased energy transfer is sufficient to completely fill the viscous deficit and instead creates a region with a pressure coefficient greater than 1, resulting in a slight thrust effect. The position of the wake is also indicative of the influence the circulation control setup has on the flowfield. The wake is positioned further downward (negative y) with respect to the aerofoil chord line due to the greater level of streamline curvature that can be sustained as the jet momentum increases.

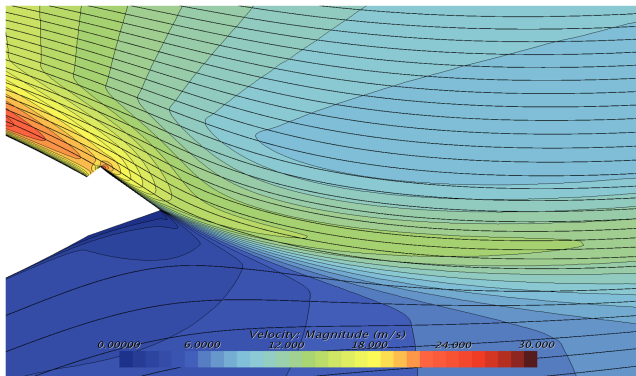


Figure 24: Velocity flowfield and streamlines for the optimised geometry at a C_{μ} value of 0.4 and 30° angle of attack

The effect of decreasing the required pressure drop acts to move the optimal geometry point towards an aerofoil exhibiting an increased thickness to chord and NACA leading edge index parameter, effectively preferring a thicker aerofoil with a more rounded, larger radius leading edge. The increased C_{μ} value allows the jet to remain attached to this more rounded leading edge at a consistent angle of attack and the increased streamline curvature result in a larger lift coefficient across all tested cases.

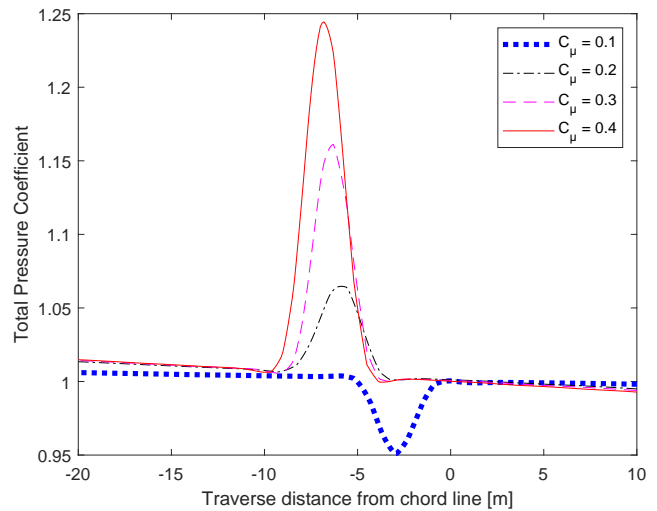


Figure 25: Variation of wake total pressure coefficient over a C_{μ} range between of 0.1 and 0.4

5. Conclusions

This work optimised the shape of a coflow jet style circulation control aerofoil with application to ship wind propulsion. The aerofoil employs blowing from the leading edge and suction near the trailing edge as a means of energising the boundary layer and creating high lift with low drag.

A preliminary study concerned with validating the computational model found good agreement with previously published aerodynamic wind tunnel data for coflow jet style aerofoils. Having established a sufficiently accurate computational fluid dynamics model, the Spallart-Allmaras model was applied to the ship wind assisted propulsion (SWAP) geometry.

Using a Kriging model trained on a 30 point Latin hyper cube has been shown to accurately capture trends between input parameters and aerodynamic outputs for circulation control aerofoils. The angle of attack, α_{oa} , and blowing momentum coefficient, C_{μ} , were mapped to lift coefficient and pressure drop with sufficient accuracy for exploitation using a genetic algorithm for optimisation.

The method allowed for fast evaluation of the sensitivity of results to wind speed with an average increase in maximum lift coefficient of 13.17% achieved over the three different velocities tested. The maximum lift coefficient increase was found to be 15.67% at a freestream velocity of 10 m/s. Lift coefficient increases of 15.05% and 8.78% were found at freestream velocities of 8 m/s and 12 m/s respectively, showing that the optimised aerofoil offered a robust performance curve and had no sharp drop-offs in performance over the required operating range.

Due to circulation control wings having multiple parameters essential to their performance, such as jet and suction locations and widths, concessions were made in parametrisation of the aerofoil shape. The outer surface of the aerofoil was constrained by the NACA framework and

must represent a NACA section, although there is no confirmation that a NACA section is optimal for the considered design problem. Further work may consider a higher order method for definition of the wing outer surface.

Although the aerofoil exhibits significant performance increases, it is thought that there is additional performance in the system and further study may provide an increased objective function benefit. The 30 point Latin hypercube used to initially train the Kriging function which maps geometric inputs to performance metrics is considered small for an 8 dimensional optimisation problem. Further work may consider increasing this initial training data set as well as employing an optimisation approach which combines pure exploitation of the objective function with a combined exploration/exploitation approach.

As noted in previous studies it is expected that optimisation with reference to a specific craft will reveal further possible fuel savings. Pairing parameters such as ship type, size, speed and voyage routes with the ship wind assisted propulsion device studied here is an area for future research. Similarly, a study into the interaction effects between aerofoils when multiple devices are in situation on board a ship deck is also important in quantifying the overall performance benefit and fuel savings.

6. Acknowledgments

The work presented in this paper has been carried out under a research scholarship jointly funded by the University of Glasgow, SMAR Azure LTD and the Energy Technology Partnership (ETP). Results were obtained using the ARCHIE-WeSt High Performance Computer (www.archie-west.ac.uk) based at the University of Strathclyde. We thank Neil Adams for his useful discussions and technical input when constructing the optimisation routine.

References

- Andino, M.Y., Lin, J.C., Roman, S., Graff, E.C., Gharib, M., Whalen, E.A., Wagnanski, I.J., 2019. Active flow control on vertical tail models. *AIAA Journal* 57, 3322–3338. doi:doi:10.2514/1.J057876.
- Atkinson, G., Nguyen, H., Binns, J., 2018. Considerations regarding the use of rigid sails on modern powered ships. *Cogent Engineering* 5, 1543564. doi:doi:10.1080/23311916.2018.1543564.
- Bardina, J.E., Huang, P.G., Coakley, T.J., 1997. Turbulence modeling validation, testing, and development. *NASA technical memorandum* 110446, 147.
- Cames, M., Graichen, J., Siemons, A., Cook, V., 2015. Emission reduction targets for international aviation and shipping. *European Parliament's Committee on Environment, Public Health and Food Safety* URL: [https://www.europarl.europa.eu/RegData/etudes/STUD/2015/569964/IPOL_STU\(2015\)569964_EN.pdf](https://www.europarl.europa.eu/RegData/etudes/STUD/2015/569964/IPOL_STU(2015)569964_EN.pdf).
- Carmichael, R., 2001. Algorithm for calculating coordinates of cambered naca airfoils at specified chord locations, in: *1st AIAA, aircraft, technology integration, and operations forum*, p. 5235. doi:doi:10.2514/6.2001-5235.
- Carter, R.A., 2006. Boat remains and maritime trade in the persian gulf during sixth and fifth millennia bc. *Antiquity* 80, 52–63. doi:doi:10.1017/S0003598X0009325X.
- Carter, W.E., Carter, M.S., 2010. The age of sail: A time when the fortunes of nations and lives of seamen literally turned with the winds their ships encountered at sea. *Journal of Navigation* 63, 717–731. doi:doi:10.1017/S0373463310000263.
- Charrier, B., Constans, J., Cousteau, J.Y., Daif, A., Malavard, L., Quinio, J.L., 1985. Fondation cousteau and windship propulsion 1980 – 1985 system cousteau - pechiney. *Journal of Wind Engineering and Industrial Aerodynamics* 20, 39 – 60. doi:doi:https://doi.org/10.1016/0167-6105(85)90011-X.
- Chrzanowski, I., 1980. Shipping in the 1980s—a future with uncertainty? *Maritime Policy & Management* 7, 1–8. doi:doi:10.1080/03088838000000048.
- Coanda, H., 1936. Device for deflecting a stream of elastic fluid projected into an elastic fluid. *US Patent* 2,052,869.
- Copuroglu, H.I., Pesman, E., 2018. Analysis of flettner rotor ships in beam waves. *Ocean Engineering* 150, 352–362. doi:doi:https://doi.org/10.1016/j.oceaneng.2018.01.004.
- Craft, T., Johnson, N., Launder, B., 2014. Back to the future? a re-examination of the aerodynamics of flettner-thom rotors for maritime propulsion. *Flow, turbulence and combustion* 92, 413–427. doi:doi:10.1007/s10494-013-9486-4.
- Dadd, G., Hudson, D., Sheno, R., 2011. Determination of kite forces using three-dimensional flight trajectories for ship propulsion. *Renewable Energy* 36, 2667–2678. doi:doi:10.1016/j.renene.2011.01.027.
- Ewing, P., 2015. Best practices for aerospace aerodynamics, in: *STAR East Asia Conference*. URL: <http://mdx2.plm.automation.siemens.com/presentation/workshop-ii-best-practices-aerospace-aerodynamics-modeling>.
- Forrester, A., Sobester, A., Keane, A., 2008. Constructing a Surrogate. *John Wiley and Sons Ltd*. chapter 2. pp. 33–76. doi:doi:https://doi.org/10.1002/9780470770801.ch2.
- Guerri, O., Erwan, L., Hamdouni, A., 2016. Numerical simulation of the turbulent flow around an oval-sail. *Journal of Applied Fluid Mechanics* 9, 2009–2023. doi:doi:10.18869/acadpub.jafm.68.235.24117.
- Hcini, C., Abidi, E., Kamoun, B., Afungchui, D., 2016. Numerical prediction for the aerodynamic performance of turbosail type wind turbine using a vortex model. *Energy* 109, 287–293. doi:doi:10.1016/j.energy.2016.04.113.
- Hoffmann, J., Sirimanne, S., 2017. Review of maritime transport, 2017. *Technical Report*. United Nations.
- Joung, T.H., Kang, S.G., Lee, J.K., Ahn, J., 2020. The imo initial strategy for reducing greenhouse gas(ghg) emissions, and its follow-up actions towards 2050. *Journal of International Maritime Safety, Environmental Affairs, and Shipping* 4, 1–7. doi:doi:10.1080/25725084.2019.1707938.
- Ju, Y., Zhang, C., 2012. Multi-point robust design optimization of wind turbine airfoil under geometric uncertainty. *Proceedings of the Institution of Mechanical Engineers, Part A: Journal of Power and Energy* 226, 245–261. doi:doi:10.1177/0957650911426540.
- Keramat, M., Kielbasa, R., 1997. Latin hypercube sampling monte carlo estimation of average quality index for integrated circuits. *Analog Integrated Circuits and Signal Processing* 14, 131–142. doi:doi:10.1023/A:1008207113480.
- Kukner, A., Bulut, S., Halilbese, A., 2016. Renewable energy options and an assessment of wind-based propulsion systems for small crafts, in: *Naval Academy Scientific Bulletin*. doi:doi:10.21279/1454-864X-16-12-006.
- Lang, M., 2006. Globalization and its history. *Journal of Modern History* 78, 899–931. doi:doi:10.1086/511251.
- Lee, H., Jo, Y., Lee, D., Choi, S., 2016. Surrogate model based design optimization of multiple wing sails considering flow interaction effect. *Ocean Engineering* 121, 422–436. doi:doi:10.1016/j.oceaneng.2016.05.051.
- Lophaven, S.N., Nielsen, H.B., Søndergaard, J., et al., 2002. DACE: a Matlab kriging toolbox. volume 2. Citeseer.
- Lu, R., Ringsberg, J., 2020. Ship energy performance study of three wind-assisted ship propulsion technologies including a parametric study of the flettner rotor technology. *Ships and Offshore Structures* 15, 249–258. doi:doi:10.1080/17445302.2019.1612544.
- Menter, F.R., Kuntz, M., Langtry, R., 2003. Ten years of industrial experience with the sst turbulence model. *Turbulence, heat and mass transfer* 4, 625–632.

- Naaijen, P., Koster, V., 2007. Performance of auxiliary wind propulsion for merchant ships using a kite, in: 2nd International Conference on Marine Research and Transportation, pp. 45–53.
- Ouchi, K., Uzawa, K., Kanai, A., Katori, M., 2013. Wind challenger” the next generation hybrid sailing vessel, in: The Third International Symposium on Marine Propulsors, Launceston, Tasmania, Australia, pp. 562–567.
- Paiva, R.M., Carvalho, A.R., Crawford, C., Suleman, A., 2010. Comparison of surrogate models in a multidisciplinary optimization framework for wing design. *AIAA Journal* 48, 995–1006. doi:doi:10.2514/1.45790.
- Park, K., Oh, P.K., Lim, H.J., 2006. The application of the cfd and kriging method to an optimization of heat sink. *International Journal of Heat and Mass Transfer* 49, 3439–3447. doi:doi:10.1016/j.ijheatmasstransfer.2006.03.009.
- Reba, I., 1966. Applications of the coanda effect. *Scientific American* 214, 84–93.
- Rodman, L.C., Wood, N., Roberts, L., 1989. Experimental investigation of straight and curved annular wall jets. *AIAA journal* 27, 1059–1067. doi:doi:10.2514/3.10221.
- Rojon, I., Dieperink, C., 2014. Blowin’ in the wind? drivers and barriers for the uptake of wind propulsion in international shipping. *Energy Policy* 67, 394–402. doi:doi:10.1016/j.enpol.2013.12.014.
- Rumsey, C., 2016. Model readiness rating system. URL: <https://turbmodels.larc.nasa.gov/modelreadiness.html>.
- Rumsey, C., 2020. 2d coflowing jet verification. URL: <https://turbmodels.larc.nasa.gov/shear.html>.
- Rutkowski, G., 2016. Study of green shipping technologies-harnessing wind, waves and solar power in new generation marine propulsion systems. *TransNav: International Journal on Marine Navigation and Safety of Sea Transportation* 10, 627–632. doi:doi:10.12716/1001.10.04.12.
- Searcy, T., 2017. Harnessing the wind: A case study of applying flettner rotor technology to achieve fuel and cost savings for fiji’s domestic shipping industry. *Marine Policy* 86, 164–172. doi:doi:10.1016/j.marpol.2017.09.020.
- Shankara, P., Snyder, D., 2012. in: Numerical simulation of high lift trap wing using STAR-CCM+. doi:doi:10.2514/6.2012-2920.
- Shur, M.L., Strelets, M.K., Travin, A.K., Spalart, P.R., 2000. Turbulence modeling in rotating and curved channels: Assessing the spalart-shur correction. *AIAA Journal* 38, 784–792. doi:doi:10.2514/2.1058.
- Siemens, P., 2018. Software (2018) star-ccm+ documentation version 13.06.
- SkySails, 2020. V-per vessel performance management: Skysails marine performance. URL: <https://www.skysails-mp.com/vper-product.html>.
- Smirnov, P.E., Menter, F.R., 2009. Sensitization of the sst turbulence model to rotation and curvature by applying the spalart-shur correction term. *Journal of turbomachinery* 131. doi:doi:10.1115/1.3070573.
- Spalart, P., Allmaras, S., 1992. A one-equation turbulence model for aerodynamic flows. *AIAA Journal* 439. doi:doi:10.2514/6.1992-439.
- Suominen, T., 2015. in: Rotor pilot project on M/S Estraden of Bore fleet, Satakunnan ammattikorkeakoulu.
- Traut, M., Gilbert, P., Walsh, C., Bows, A., Filippone, A., Stansby, P., Wood, R., 2014. Propulsive power contribution of a kite and a flettner rotor on selected shipping routes. *Applied Energy* 113, 362–372. doi:doi:10.1016/j.apenergy.2013.07.026.
- Viola, I.M., Sacher, M., Xu, J., Wang, F., 2015. A numerical method for the design of ships with wind-assisted propulsion. *Ocean Engineering* 105, 33–42. doi:doi:10.1016/j.oceaneng.2015.06.009.
- Yaras, M., Grosvenor, A., 2002. An evaluation of several low-re turbulence models part 1-flat-plate boundary layer and axisymmetric separating flows, in: ICAS 2002 Congress.
- Zha, G.C., Carroll, B.F., Paxton, C.D., Conley, C.A., Wells, A., 2007a. High-performance airfoil using coflow jet flow control. *AIAA journal* 45, 2087–2090. doi:doi:10.2514/1.20926.
- Zha, G.C., Gao, W., Paxton, C.D., 2007b. Jet effects on coflow jet airfoil performance. *AIAA Journal* 45, 1222–1231. URL: <https://doi.org/10.2514/1.23995>, doi:doi:10.2514/1.23995.
- Zou, Y.L., Hu, F.L., Zhou, C.C., Li, C.L., Dunn, K.J., 2013. Analysis of radial basis function interpolation approach. *Applied geophysics* 10,